Stochastic geomorphological transport for terrain erosion simulation

NICHOLAS MCDONALD, erosiv Studio GmbH, Austria
GUILLAUME CORDONNIER, Centre Inria d'Université Côte d'Azur, France

Mountainous terrains evolve over geological timescales through erosion processes driven by the complex interplay of transported quantities such as water, sediment, and rockfall. A key challenge in erosion modeling is the simultaneous simulation of transport and erosive processes, which differ in temporal scales by several orders of magnitude. We address this challenge with a novel, parallel, stochastic particle-based method capable of simulating transport over geological timescales. Our approach relaxes the strong assumptions on velocity required by prior works (*e.g.*, based on the Stream Power Law), enabling a new erosion model grounded in a more general form of momentum conservation. We demonstrate that our scheme accurately solves the underlying conservation laws and avoids artifacts common in previous works. Furthermore, we show that our new erosion model captures multiscale geomorphological features, producing coherent basin structures and dynamic phenomena such as braided rivers, meanders, and deltas.

CCS Concepts: • **Computing methodologies** → **Massively parallel and high-performance simulations**; **Massively parallel algorithms**; **Shape modeling**; **Shape modeling**; • **Applied computing** → **Earth and atmospheric sciences**.

Additional Key Words and Phrases: Terrain, Erosion, Transport, Lagrangian Simulation, Grid-Free Monte Carlo

ACM Reference Format:
Nicholas McDonald and Guillaume Cordonnier. 2026. Stochastic geomorphological transport for terrain erosion simulation. *ACM Trans. Graph.* 45, 4, Article 78 (July 2026), 12 pages. https://doi.org/10.1145/3811336

1 INTRODUCTION

Mountainous landscapes are prominent features in virtual environments. However, synthesizing realistic digital mountain landscapes suffers from several challenges inherited from the geological complexity of their real-world counterparts.

Prior work enforces geomorphological consistency either *locally* using procedural techniques [Guérin et al. 2022] and machine learning models [Lochner et al. 2023], or *globally* through physics-based simulations [Benes 2007]. In particular, physics-based models inspired by geological processes – such as those employing the Stream Power Law to simulate fluvial erosion [Cordonnier et al. 2016] – are well-suited for generating large-scale terrains. However, their efficiency relies on specific graph traversal strategies that impose restrictive assumptions, notably that water flow strictly follows the steepest topographic gradients. This constraint limits the expressiveness of the model and its ability to reproduce complex phenomena such as meandering rivers, braided channels, deltas, or generalize to other processes like rockfalls. Furthermore, their reliance on Eulerian grid-based discretization induces salient directional artifacts and a strong dependence on resolution.

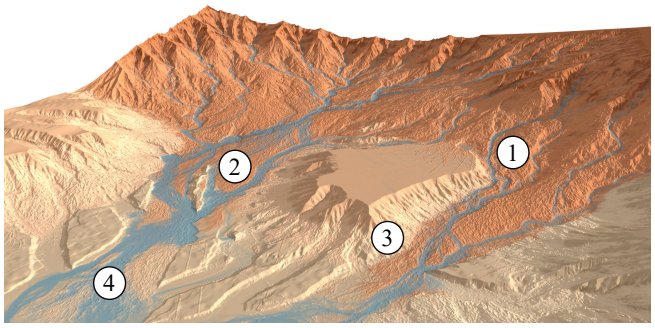

Fig. 1. Our new algorithm for geomorphological transport models complex transports with momentum conservation for terrain erosion, resulting in the emergence of complex terrain features such as meanders (1), braided rivers and deltas (2), debris flow scars (3), and alluvial fans (4).

We observe that momentum conservation drives the emergence of characteristic landforms. Momentum terms induce inertial curvatures in meandering rivers [Paris et al. 2023], while momentum instabilities with sediment overloading dictate the separation of braided rivers [Ashmore 1991] and deltas [Jerolmack and Mohrig 2007]. Momentum enables the propagation of rockfalls and debris-flows [Iverson 1997] beyond their angle of repose and governs their erosive capacity. This observation motivates the need for a numerical scheme for long-distance transport compatible with velocities obtained – and transported – through momentum conservation.

We define *geomorphological transport* as the displacement of quantities (e.g., water flow thickness, sediment concentration, debris flow mass, velocity) across a terrain over geological time scales -— that is, durations significantly longer than the characteristic time for a particle to traverse the domain. To model this transport, we introduce a novel numerical scheme based on a stochastic, particle-based formulation. We prefer particles over traditional Eulerian approaches that often suffer from numerical diffusion and directional artifacts. Additionally, the stochastic sampling of the particles introduces a natural looking spatial variability.

We root our approach in a mathematical derivation from fundamental conservation laws, which ensures physical consistency and clarifies the assumptions required for this model. This formulation also enables the design of an efficient, parallelizable algorithm agnostic to the nature of the transported quantity.

To demonstrate the versatility and effectiveness of our approach, we formulate a new erosion model that generalizes state-of-the-art formulations based on the Stream Power Law and debris flow. Our model incorporates momentum conservation by directly transporting the velocity field through the geomorphological transport

Authors' addresses: Nicholas McDonald, erosiv Studio GmbH, Vienna, Austria, nick@erosiv.studio; Guillaume Cordonnier, Centre Inria d'Université Côte d'Azur, Nice, France, guillaume.cordonnier@inria.fr.

ACM 0730-0301/2026/7-ART78
https://doi.org/10.1145/3811336

framework. Using our particle-based scheme, we show through various examples that this model captures the emergence of terrain features previously unrepresented in erosion simulations (Fig. 1).

In summary, our contributions are 1) a new terrain erosion model that generalizes fluvial erosion (Stream Power Law) and debris-flow entrainment with momentum conservation, 2) a parallel, stochastic, particle-based scheme for geomorphological transport compatible with complex velocity fields, and 3) a full mathematical derivation that embeds our solver in the fundamental mass- and momentum-conservation equations. An open-source implementation is publicly available under https://github.com/erosiv/geotransport.

2 RELATED WORK

Since the pioneering work by Musgrave et al. [1989], terrain generation relies on approaches ranging from procedural methods [Ebert et al. 2002; Guérin et al. 2022] to example-based synthesis [Gain et al. 2015; Zhou et al. 2007], machine learning [Guérin et al. 2017; Lochner et al. 2023; Perche et al. 2023], or simulation. Each of these methods excels at reproducing terrain features at a specific scale. In this work, we focus on simulation-based methods for generating consistent large-scale terrains up to the extent of the mountain range. We refer the reader to the survey by Galin et al. [2019] for a review of the alternative approaches.

A challenge in simulation-based methods is to manage the interaction of the diverse physical processes driving landscape evolution, such as tectonic uplift and fluvial erosion [Cordonnier et al. 2016, 2017a; Schott et al. 2023], the impact of vegetation [Cordonnier et al. 2017b], glaciers [Cordonnier et al. 2023], or debris-flows [Jain et al. 2024a]. These interactions are especially complex when phenomena operate across distinct temporal scales, for instance in transport-based erosion where erosion results from the slow abrasion caused by fast-moving materials such as water or falling rocks [Chen et al. 2014]. Water may traverse a mountainous landscape in days, but a mountain forms over millions of years. In the following, we review strategies adopted in computer graphics to estimate the transported quantities and couple transport with erosion.

Local fluid dynamics. A direct approach to modeling transport phenomena is to simulate local fluid exchanges between neighboring cells. This strategy forms the backbone of *hydraulic erosion* methods, dating back to the first erosion algorithms [Musgrave et al. 1989], and has since been enhanced with sediment layers [Benes and Forsbach 2001] or accelerated on the GPU [Vanek et al. 2011]. This local approach is straightforward to implement and incorporate physically accurate models for both erosion processes [Wojtan et al. 2007] and fluid dynamics [Benes 2007; Krištof et al. 2009]. However, transport based on fluid dynamics requires small time steps for numerical stability, and limits the applicability of these approaches to small domains, often limited to tens of meters in extent.

Global discharge-based models. In contrast, fluvial erosion models from geomorphology [Howard and Kerby 1983; Whipple and Tucker 1999] forgo detailed fluid dynamics and extract flow properties directly from the terrain slope and water discharge. Discharge, the volumetric flow rate within a river network, can be estimated as the upstream accumulation of precipitation. As a result, these models require only a topological traversal of the terrain to compute discharge, and enable large time steps suitable for simulating landscape evolution at geological scales [Braun and Willett 2013; Cordonnier et al. 2016]. This approach has been extended in multiple directions: for increased user control [Cordonnier et al. 2017a], for terrain reconstruction via reverse erosion [Yang et al. 2024], for instantaneous erosion using analytical solutions [Steer 2021; Tzathas et al. 2024], and to account for debris-flow erosion typical of steep slopes [Jain et al. 2024a]. Parallel and GPU implementations are challenging, since discharge depends non-locally on precipitation. To address this, approximate solutions [Schott et al. 2023] update discharge over short local neighborhoods at each time step, but are constrained to settings where the terrain only marginally changes at each iteration. In contrast, graph reduction algorithms [Jain et al. 2024b] provide exact solutions but are constrained to single-direction flows where a cell can only propagate discharge to a single neighbor. We argue that the simplifications in these methods -— particularly the neglect of momentum conservation —— significantly constrain their expressiveness. In particular, they fail to capture key fluvial features such as meanders and braided channels, which are known to emerge from complex momentum interactions [Jerolmack and Mohrig 2007].

Lagrangian methods. While widely used in fluid simulations in computer graphics, Lagrangian methods have seen limited adoption in terrain erosion. A few exceptions exist, such as hydraulic erosion using Smoothed Particle Hydrodynamics [Krištof et al. 2009], or particle-based frameworks designed to integrate multiple processes and data structures [Hartley et al. 2024]. Note that particle-based systems are common in industrial software (Gaea [QuadSpinner 2025], World Machine [Software 2025]), with impressive results but limited implementation access, and no evidence of physical guarantees. A similar preference for Eulerian formulations is observed in geomorphology, with some exceptions such as the method of *precipitrons*, which has been used to simulate both large-scale landscape evolution [Chase 1992] and fine-scale river morphology [Davy et al. 2017]. However, these methods primarily target short-distance transport. In contrast, our approach leverages a Lagrangian representation to model long-distance geomorphological transport over the geological time scales of the erosion of entire mountain ranges.

3 OVERVIEW

We simulate large-scale mountain erosion in a 2.5D setting. More specifically, we consider a terrain defined as an elevation field z (following the conventions from the geomorphology literature) over an open 2D domain $\Omega \subset \mathbb{R}^2$ parameterized by the horizontal coordinates $\mathbf{x} = (x, y)$ and time $t \in [0, T]$ where T is the simulation duration. Erosion result from the cumulative impact of erosive processes. We consider specifically fluvial and debris flow erosion, that we introduce in Section 4 together with their physical model and associated quantities of river flow thickness h_f, sediment thickness h_s, and debris flow thickness h_d.

Each of these quantities are transported by a velocity ($\mathbf{v}_f$ for river flow and sediments, $\mathbf{v}_d$ for debris flows). We show in Section 4.2 that the transport of these quantities, and of the velocity itself (momentum conservation) follows similar laws, under a quasi-static approximation enabled by the geomorphological time scales. We

propose a unified formulation of this transport in Section 5 and show that the solution can be expressed as an integral: the superposition over upstream contributions. Finally, we propose in Section 6 an efficient parallel Monte-Carlo scheme to evaluate these integrals, yielding our final terrain erosion simulation algorithm.

Note that we neglect the vertical variations of flow-related quantities (e.g., water velocity, sediment concentration) and approximate them using their depth-averaged values. A table of all symbols is provided in Appendix C.

4 A TRANSPORT-BASED EROSION MODEL

Previous large-scale erosion models [Cordonnier et al. 2016] relied on simplifying assumptions that constrain stream velocity to follow terrain gradients. We introduce a new physical model that generalizes classical erosion laws and reformulates erosion mechanisms – including momentum conservation – as unified transport processes.

4.1 Fluvial and debris flow erosion

Mountain formation is driven by the balance between tectonic uplift $\mathcal{U}$, fluvial erosion $\mathcal{E}_f$, landslides $\mathcal{E}_l$, erosion by debris flows $\mathcal{E}_d$, and the deposition of sediments $\mathcal{D}_f$ and debris $\mathcal{D}_d$ [Jain et al. 2024a]. We express this balance as the evolution of elevation z:

$$\frac{\partial z}{\partial t} = \mathcal{U} - \mathcal{E}_f + \mathcal{D}_f - \mathcal{E}_d - \mathcal{E}_l + \mathcal{D}_d. \tag{1}$$

Erosion starts on a user-provided initial terrain z_0 at time $t = 0$. We use Dirichlet boundary conditions, but our method can easily accommodate Neumann or periodic behaviours at the bounds.

Fluvial erosion. Fluvial erosion refers to the mechanical abrasion by water and drives the formation of the main valleys (inset image[1], (1)). Previous works [Cordonnier et al. 2016; Schott et al. 2023] rely on the Stream Power Law [Whipple and Tucker 1999], which expresses fluvial erosion as a function of water discharge and local slope. This formulation assumes that flow velocity scales as a power law of local slope and discharge, while we will obtain more accurate velocities from momentum conservation. Therefore, we return to the original derivation of the Stream Power Law (shear stress variant) for an erosion equation that depends on velocity explicitly. Fluvial erosion $\mathcal{E}_f$ then depends on the wall shear stress τ_f, erosion coefficient k_f and exponent a:

$$\mathcal{E}_f = k_f \tau_f^a, \tag{2}$$

The velocity $\mathbf{v}_f$ appears in the wall shear stress, along with the Darcy-Weisbach friction factor f_D [Chaudhry 1979] (which we assume constant in mountain streams), water density ρ_f, and flow velocity $\mathbf{v}_f$:

$$\tau_f = \frac{1}{8} f_D \rho_f \|\mathbf{v}_f\|^2. \tag{3}$$

Sediments eroded by fluvial processes are transported downstream and deposited when the sediment load exceeds the transport capacity of the flow. Yuan et al. [2019] expressed this capacity as the ratio of sediment volumetric flow rate to discharge. We reformulate this relationship in terms of flow thickness h_f and transported sediment thickness h_s, controlled by a deposition coefficient $k_{d,f}$:

$$\mathcal{D}_f = k_{d,f} \frac{h_s}{h_f}. \tag{4}$$

Debris flows. Debris flows are a mixture of mud, water, and rock, mobilized during extreme weather events. Debris flows occur primarily on steep slopes, leaving characteristic erosion scars (inset image, (2)). Note that we use debris flows to represent a broader class of gravity-driven processes such as landslides or rockfalls, since the constitutive equations of debris flows capture material behaviors that range from dry granular flows to saturated mixtures.

We refer to *landslide erosion* – also referred to as thermal erosion in the graphics literature – as the initiating process of debris flows, occurring when a saturated mixture of mud and rocks becomes unstable and moves downslope. This process occurs when the terrain slope exceeds the material's angle of repose θ [Iverson 1997]:

$$\mathcal{E}_l = k_l \rho_d g \left(\|\nabla z\| - \tan\theta\right)_+, \tag{5}$$

where $\|\nabla z\|$ is the local topographic slope, g is gravitational acceleration, ρ_d is the debris mixture density, k_l a constant erosion coefficient, and the subscript + clamps to positive values.

Jain et al. [2024a] showed that the visual impact of debris flow goes beyond the slope-reducing effect of debris flow initiation: the movement of debris leaves erosion scars on steep slopes. Similar to fluvial erosion, their approach relies on simplifying assumptions that remove the velocity term from the governing equations. In contrast, we adopt a geophysical model [Iverson and Ouyang 2015] that expresses debris-flow erosion and deposition as a force balance normalized by the flow velocity $\mathbf{v}_d$:

$$\mathcal{E}_d = k_d \frac{(\rho_d g h_d \|\nabla z\| - \tau_d)_+}{\rho_d \|\mathbf{v}_d\|}, \tag{6}$$

$$\mathcal{D}_d = k_{d,d} \frac{(\tau_d - \rho_d g h_d \|\nabla z\|)_+}{\rho_d \|\mathbf{v}_d\|}, \tag{7}$$

where h_d is the debris flow thickness, and k_d and $k_{d,d}$ constant coefficients. While Jain et al. [2024a] required numerical limiters to control the amount of deposited debris, our deposited debris progressively propagates beyond the angle of repose thanks to the flow momentum. Note that we set $\mathcal{D}_d$ to 0 if $h_d = 0$.

The wall shear stress τ_d mixes the solid and fluid components of the debris flow by incorporating a solid (Mohr-Coulomb) and viscous (Bingham) components:

$$\tau_d = \left(\tau_y + \rho_d g h_d \tan\theta + \mu_d \frac{\|\mathbf{v}_d\|}{h_d}\right), \tag{8}$$

where τ_y is the (constant) yield stress and μ_d the mixture viscosity.

Erosion as Transport. The fluvial and debris-flow erosion rates have in common that they depend only on material parameters and quantities transported across the terrain: the flow velocities $\mathbf{v}_f$, $\mathbf{v}_d$, the flow thicknesses h_f, h_d, and the sediment thickness h_s. In the following section, we will show how these quantities are modeled by similar transport equations.

[1] Chancellor Peak, Canadian Rockies. Image from Google Earth, Attribution: Maxar Technologies, Landsat / Copernicus, CNES, Airbus.

4.2 Geomorphological Transport

Landscapes are eroded with Eq. 1 over several thousand years by transported quantities (water, sediment, debris) that traverse the whole extent of the terrain within days. This significant difference in time scales leads us to introduce the concept of *geomorphological transport*. We define *geomorphological transport* as the transport of elements across a terrain, evaluated over geological timescales, with two key properties:

(1) *Quasi-static transport.* Given that topographic variations are negligible in the transport timescale, we assume that the velocities and quantities of the transported materials do not vary in time *locally* (in the Eulerian meaning, *i.e.*, $\partial/\partial t \approx 0$).
(2) *Long distance transport.* A consequence of the *quasi-static* assumption is that the transport does not depend on time. Therefore, all transported quantities travel from their source to the bounds of the domain within a simulation timestep.

The *long-distance transport* assumption explains the algorithmic difficulty of coupling erosion and transport, where, at each erosion time step, the transported quantities need to be updated across the entire landscape. In this work, we leverage these two properties to propose a new and efficient solution for geomorphological transport.

Water transport. Water accumulates from precipitation p_f, flows over the terrain at velocity $\mathbf{v_f}$, and disappears from the combined effect of vegetation uptake and evaporation. We model this process, called *evapotranspiration* [Guswa et al. 2002], with a constant rate k_e.

$$\frac{\partial h_f}{\partial t} + \nabla \cdot \left(\mathbf{v}_f h_f\right) = p_f - k_e\, h_f. \tag{9}$$

We rewrite Eq. 9 with the quasi-static transport property – which we will assume from now on:

$$\nabla \cdot \left(\mathbf{v}_f h_f\right) = p_f - k_e\, h_f. \tag{10}$$

Sediment and debris transport. Sediment produced by fluvial erosion and debris mobilized in debris flows share similar characteristics: both result from the net balance between erosion and deposition, and are carried downstream by the surrounding flow. Therefore, we model both phenomena with the same transport equation, where $(\mathbf{v}, h, \mathcal{E}, \mathcal{D})$ stands for $(\mathbf{v}_f, h_s, \mathcal{E}_f, \mathcal{D}_f)$ for sediments, and $(\mathbf{v}_d, h_d, \mathcal{E}_d + \mathcal{E}_l, \mathcal{D}_d)$ for debris flows. The material derivative is taken along $\mathbf{v}_f$ and $\mathbf{v}_d$, respectively.

$$\nabla \cdot (\mathbf{v}h) = \mathcal{E} - \mathcal{D} \tag{11}$$

Momentum conservation. Both rainwater and debris-flow velocities are governed by momentum conservation. As above, we express their dynamics using generic variables: $(\mathbf{v}, h, \rho, \tau, \mu)$ denoting, respectively, the velocity, thickness, density, basal shear stress, and dynamic viscosity of either rainwater or debris flows.

As is common in depth-averaged modes [LeVeque 2002], pressure and gravity forces reduce to a slope-induced driving force $-g\nabla z$ under hydrostatic approximation:

$$\nabla \cdot (\mathbf{v}\mathbf{v}) = -g\nabla z + \frac{\mu}{\rho}\Delta \mathbf{v} - \frac{\mathbf{v}}{\|\mathbf{v}\|}\frac{\tau}{\rho h}. \tag{12}$$

Note that previous erosion laws, such as the stream power law, neglect the inertial terms (left-hand side of Eq. 12) and solve the balance between gravity and friction forces (first and last terms of the right-hand side), which yields a local expression for the velocity. Incorporating momentum and viscosity allows the formation of patterns such as meanders and braids (inset image, (3)).

5 TRANSPORT OF UPSTREAM CONTRIBUTIONS

We previously introduced the governing equations of our erosion model, which depend on quantities (mass, momentum) that are transported across the terrain. Importantly, the transport equations (Eqs. 10 to 12) share the common form of a linear (or linearizable) conservation law. This motivates a unified method for the solution of such transport equations. In this section, we introduce the mathematical basis underlying a new algorithm for the simulation of geomorphological transport.

Our primary assumption of geomorphological transport states that, at a given time t, a transported quantity ϕ varies sufficiently quickly relative to the erosion time scale to reach a quasi-static steady state. We express this state as the solution of the general quasi-static linear conservation law:

$$\nabla \cdot (\phi \mathbf{v}) = S - R\,\phi \tag{13}$$

where $\mathbf{v}$ is the velocity, and R and S material decay and source, respectively. Our goal is to evaluate the quantity ϕ, to use it later in our explicit erosion model. We will now solve Eq. 13 by expressing $(\phi\mathbf{v})$ as the *superposition of attenuated upstream contributions* – an integral easily evaluated with a stochastic solver (Section 6).

Disentangling Source and Decay. Taking water transport as an example, an *attenuated upstream contribution* would correspond to a droplet of water – or more precisely a precipitation rate S – that is sourced at position $\mathbf{y}$, and progressively decays by a factor R (evaporation) as it is transported. This droplet eventually reaches a point $\mathbf{x}$ where it accumulates with other upstream contributions to form a river, where we compute $\phi(\mathbf{x})$.

To combine all upstream contributions at a position x following this intuition, a solution is to isolate each (attenuated) contribution of the source S at each upstream position y. This equivalently requires us to disentangle the effect of the source S from the effect of the decay R in our quasi-static conservation law.

We achieve this disentanglement by first isolating the cumulative decay and introducing the *attenuation function* M:

$$\mathbf{v} \cdot \nabla M = -R\,M. \tag{14}$$

Note the operator $\mathbf{v} \cdot \nabla$, which indicates that M models the cumulative decay along a *streamline* (curve traced by following the velocity $\mathbf{v}$). To make the streamline dependence explicit, we introduce the notation $\mathbf{y} \rightarrow \mathbf{x}$ to denote a pair of points $(\mathbf{y}, \mathbf{x}) \in \Omega^2$ such that $\mathbf{y}$ and $\mathbf{x}$ are on the same streamline and $\mathbf{y}$ is upstream of $\mathbf{x}$.

Note that M is defined up to a multiplicative constant. We ignore this ambiguity as we exclusively use M in the *attenuation ratio* α

$$\alpha(\mathbf{y} \rightarrow \mathbf{x}) = \frac{M(\mathbf{x})}{M(\mathbf{y})}, \tag{15}$$

which represents the cumulative decay from a position $\mathbf{y}$ to a downstream position $\mathbf{x}$ along the same streamline. We can now define the *attenuated upstream contribution* $\hat{\phi}(\mathbf{y} \rightarrow \mathbf{x})$ as the contribution

of the source term at $\mathbf{y}$ attenuated down to $\mathbf{x}$:

$$\hat{\phi}(\mathbf{y} \to \mathbf{x}) = S(\mathbf{y})\alpha(\mathbf{y} \to \mathbf{x}) \tag{16}$$

In this form, the attenuated upstream contribution is a product of the upstream source value $S(\mathbf{y})$ and the attenuation ratio $\alpha(\mathbf{y} \to \mathbf{x})$, meaning that the effect of the source and decay are disentangled.

Superposition Integral. We will now write the solution of Eq. 13 in integral form using $\hat{\phi}$. In particular, we are interested in the amount of material that traverses an open curve C where $\mathbf{v}$ does not vanish. Therefore, for a point $\mathbf{y}$ to be upstream of C, we introduce the notations $\hat{\phi}_C(\mathbf{y}) = \hat{\phi}(\mathbf{y} \to \mathbf{x}_C)$ and $\alpha_C(\mathbf{y}) = \alpha(\mathbf{y} \to \mathbf{x}_C)$, where $\mathbf{x}_C$ is the intersection between C and the streamline passing through $\mathbf{y}$ (inset Figure).

We do not integrate Eq. 13 directly, as the unknown ϕ appears in the right-hand side. Instead, we observe that (proof in Appendix A):

$$\nabla_{\mathbf{y}} \cdot (\alpha_C(\mathbf{y})\phi(\mathbf{y})\mathbf{v}(\mathbf{y})) = \hat{\phi}_C(\mathbf{y}), \tag{17}$$

where $\nabla_{\mathbf{y}}$ indicates that the divergence is taken along $\mathbf{y}$.

We can now apply the divergence theorem to accumulate the upstream contributions. Given the curve C defined earlier, we construct a domain Ω_C as the set of streamlines that pass through C (inset Figure). By construction, the bound of this domain is either 1. where $\mathbf{v} = \mathbf{0}$, 2. along $\mathbf{v}$, 3. on C, or 4. on an inflow boundary condition. We ignore for now the latter (we explain how we handle inflow boundaries in Appendix B). Then,

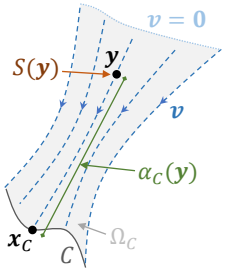

$$\int_C \phi(\mathbf{x})\mathbf{v}(\mathbf{x}) \cdot \mathbf{dl}_{\mathbf{x}} = \int_{\Omega_C} \hat{\phi}_C(\mathbf{y})\, dA_{\mathbf{y}}, \tag{18}$$

where $\mathbf{dl}_{\mathbf{x}}$ denotes a small element of length oriented toward the normal to C at $\mathbf{x}$ and $dA_{\mathbf{y}}$ an element of surface. Note that, on C, $\alpha_C(\mathbf{x}) = \alpha(\mathbf{x} \to \mathbf{x}) = 1$, which is why the ratio vanishes from the left-hand side.

Eq. 18 is our *superposition integral*, expressing the flux of ϕ through C (*e.g.*, discharge, in the case of water) as a superposition of attenuated upstream contributions $\hat{\phi}_C$ – an integral of the upstream source (precipitation) attenuated by the cumulative decay (evaporation).

Note that the surface integral in Eq. 18 can be interpreted as a convolution, indicating that the attenuation $\alpha(\mathbf{x} \to \mathbf{y})$ is a Green's function for Eq. 13.

6 ALGORITHM AND DISCRETIZATION

Eq. 18 expresses the flux of a transported quantity satisfying a quasi-static linear conservation law through some curve C as a superposition of attenuated upstream contributions in the form of an integral. We will now evaluate ths intergal on a discretized terrain, by setting C as the outflow boundary of a discrete cell.

The full domain $\Omega \subset \mathbb{R}^2$ is discretized into cells Ω_k, where we store terrain elevations z, velocities $\mathbf{v}$, and transported quantities ϕ. Without loss of generality, we use a regular grid in our implementation.

Monte-Carlo estimate. In the discrete setting, we assume ϕ constant within each cell Ω_k and denote this value by ϕ_k. We use Eq. 18 to evaluate ϕ_k through the flux $\phi_k \mathbf{v}_k$ which leaves Ω_k. Let O_k be the set of *outflow edges* of Ω_k: an edge $c \in O_k$ if c is one of the four edges forming the bound of Ω_k, and such that $\mathbf{v} \cdot \mathbf{n}_c > 0$, with $\mathbf{n}_c$ the normal to c directed toward the exterior.

With C set as $C_k = \cup O_k$, Eq. 18 becomes:

$$\phi_k = \left(\sum_{c \in O_k} |c| \mathbf{v}_k \cdot \mathbf{n}_c \right)^{-1} \int_{\Omega_{C_k}} \hat{\phi}_{C_k}(\mathbf{y})\, dA_{\mathbf{y}}. \tag{19}$$

where $|c|$ is the length of edge c ($|c| = \Delta x$ for a regular grid of spacing Δx). We now focus on the upstream integral, which we denote as Φ_k and evaluate via Monte Carlo integration:

$$\Phi_k = \int_{\Omega_{C_k}} \hat{\phi}_{C_k}(\mathbf{y})\, dA_{\mathbf{y}} = \mathbb{E}_p \left[\frac{\hat{\phi}_{C_k}(\mathbf{y})}{p(\mathbf{y}|C_k)} \right], \tag{20}$$

where $p(y|C_k)$ is a conditional probability distribution of upstream positions $y \in \Omega_{C_k}$, conditioned on each cell.

A direct evaluation of Φ_k for each cell individually is impractical, as it would require integrating the contribution of every upstream location to every downstream cell.

Instead, we adopt a sample reuse strategy by observing that an upstream contribution $\hat{\phi}(\mathbf{y} \to \mathbf{x})$ can be reused to compute the contribution from $\mathbf{y}$ to a point $\mathbf{x}'$ downstream from $\mathbf{x}$:

$$\hat{\phi}(\mathbf{y} \to \mathbf{x}') = \hat{\phi}(\mathbf{y} \to \mathbf{x})\alpha(\mathbf{x} \to \mathbf{x}'). \tag{21}$$

A sample initiated at position $\mathbf{y}$ can be propagated to contribute to *all* downstream cells. Therefore, we do not define the conditional sampling distribution per cell, but use a joint sampling distribution $p(\mathbf{y})$ over all cells and reuse the generated samples. In practice, we adopt a uniform joint sampling distribution, $p(\mathbf{y_i}) = \mathbf{1}/|\Omega|$.

We modify the stochastic integral Eq. 20 to use the joint sampling distribution with an indicator function $\omega_k(\mathbf{y})$, set to 1 if the flowline passing through $\mathbf{y}$ traverses C_k, *i.e.* C_k is downstream from $\mathbf{y}$. We then approximate Φ_k by a mean over N samples:

$$\Phi_k \approx \frac{1}{N} \sum_i^N \frac{\hat{\phi}_{C_k}(\mathbf{y}_i)}{p(\mathbf{y}_i)} \omega_k(\mathbf{y}_i) \tag{22}$$

Note that in practice, evaluation of the indicator function is trivial for a reused sample, and will always evaluate to 1 because a reused sample only traverses downstream positions by construction.

Joint integration algorithm. We generate N samples in the full domain and integrate the sub-solutions and positions along their trajectories in parallel (Eqs. 14 and 16). As we integrate the sub-solution, we can accumulate the flux into the cells $\Omega_k \subset \Omega$ encountered along the path (implicitly evaluating the indicator function). Integration terminates if the particle leaves the domain, a maximum time is reached, or the attenuation drops below a threshold. We summarize this process in Alg.1.

Note that Alg. 1 requires the evaluation of the decay R, the source S, and the velocity $\mathbf{v}$ at arbitrary positions $\mathbf{y}_i$. In practice, we store these quantities at the center of each cell and interpolate them bilinearly. Note that the source term for momentum conservation (Eq. 12) requires the topographic gradients ∇z. To ensure a smoothly

ALGORITHM 1: Parallel Stochastic Transport Integration

$\Phi_k \leftarrow 0$
In parallel for N particles i:
$\mathbf{y}_i \sim p(\mathbf{y})$
$M_i \leftarrow 1$
$\hat{S}_i \leftarrow S(\mathbf{y}_i)/p(\mathbf{y}_i)$ `// Probability-weighted source term`
while $\mathbf{y}_i \in \Omega$ *and* $M_i \geq \epsilon$ **do**
  $\Phi_k \leftarrow \Phi_k + \hat{S}_i \cdot M_i$
  $M_i \leftarrow M_i e^{-\Delta x\, R(\mathbf{y}_i)/\|\mathbf{v}(\mathbf{y}_i)\|}$ `// Solution of Eq. 14`
  $\mathbf{y}_i \leftarrow \mathbf{y}_i + \Delta x\, \mathbf{v}(\mathbf{y}_i)/\|\mathbf{v}(\mathbf{y}_i)\|$
end
$\phi_k = \frac{1}{N}\Phi_k / \sum_{c \in C_k} |c| \mathbf{v}_k \cdot \mathbf{n}_c$

varying field, we compute the gradients per cell with an upwind scheme before interpolation.

We stress that Alg. 1 easily generalises to higher dimensions and non-regular discretizations, even with overlapping cells. In any case, care must be taken that each particle contributes to each control cell only once.

Time stepping. The geomorphological transport assumption eliminates time from the transport equations, but we still need to iterate the erosion law in Eq. 1 over a geological timestep Δt. We use Alg. 1 to solve all transport systems and iterate the erosion law as follows:

(1) Compute the erosion and deposition rates (Eqs. 2, 4, 5, 6, 7) using all quantities at time t.
(2) Evaluate flow and debris velocities at time $t + \Delta t$ from the momentum conservation law (Eq. 12) using all quantities and trajectories at time t using Alg. 1.
(3) Evaluate the transported water, sediment and debris quantities (Eqs. 10 and 11) at time $(t + \Delta t)$ using all quantities at time t and trajectories at time $t + \Delta t$ using Alg. 1.
(4) Update the surface elevation (Eq. 1) using the previously computed erosion and deposition rates.

When a transported quantity appears non-linearly in the right-end side of a transport equation, as the flow velocity in Eq. 12, which appears as $\mathbf{v}^2$ through Eq. 3, we linearize (*e.g.*, $\mathbf{v}^2 = \mathbf{v}(t + \Delta t) \cdot \mathbf{v}(t)$), and use the value from time t in the decay R. We treat $\Delta \mathbf{v}$ in Eq. 12 similarly: we discretize the Laplacian with the standard 4-neighbor stencil, obtaining all values from time t (source term) except for the value at the center, which we consider at time $t + \Delta t$ (decay term).

Filtering. At each timestep, we generate a noisy estimate for the transported quantity, which can degrade the visual quality of the terrain for a low number of upstream samples. We mitigate these issues with a temporal exponential filter (with parameter β):

$$\phi(t + \Delta t) \leftarrow \beta \phi(t + \Delta t) + (1 - \beta)\phi(t). \tag{23}$$

7 RESULTS AND VALIDATION

We implemented our method in C++/CUDA. All results were generated on a computer with an AMD Ryzen 5 9600X 6 core CPU clocked at 3.9 GHz with 64GB of RAM and an NVIDIA GeForce RTX 5070 Ti GPU with 16GB of dedicated VRAM.

We paint the initial terrain with an exaggerated color-scheme and transport the colors proportionally to the total mass suspension rate $h_s + h_d$ to show the origin of debris and sediments. We highlight the deposits with a slightly brighter albedo, and emphasize river paths with a blue color based on water thickness. This coloration has no bearing on the erosion parameters, which we keep uniform to emphasize variation by transport.

To carefully showcase the output of our algorithm, we did not add any post-process noise or texture to the height or albedo fields. Additionally, we exclusively use blank initial conditions, meaning a uniform (flat) height field and zeroed fields for the transported quantities. The only source of randomness in our model thus lies in the sampling procedure of our stochastic integral.

7.1 Convergence validation and performance

We validate the convergence of our algorithm on a simplified experiment where ground-truth is available. We simulate water transport across a convergent conical height-field of radius R according to Eq. 10, with a uniform source, no decay, and velocity proportional to the height gradient. We compare our results to the analytical solution $\phi = S/(2r\|\mathbf{v}\|)(R^2 - r^2)$ at distance r to the center.

Convergence. In Fig. 2, we compare our results with the ground truth, using the mean squared relative error (MSRE). Independent of the resolution, we observe a linear convergence for a varying sample count N to a resolution K ratio (left), until we exceed 1 sample per cell. We also observe a linear convergence when we fix $N = K$ and vary the resolution K (right).

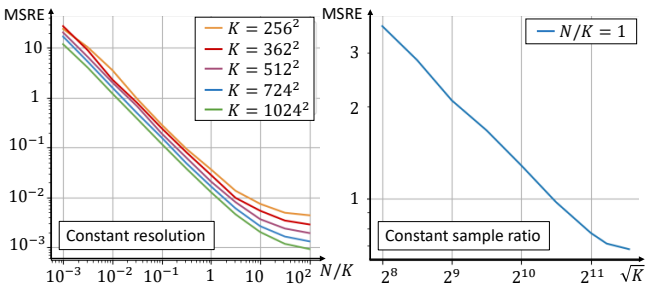

Fig. 2. Convergence plots. Left: mean squared relative error (MSRE) for varying sampling-count-to-resolution ratios. Right: Constant sampling ratio for varying resolution.

Runtime Performance. We measured the runtime performance of our algorithm for different sample counts and resolutions, reported in Table 1. We observe that the runtime is constant until the number of GPU threads becomes saturated, after which the runtime scales linearly with the number of samples. The runtime also scales linearly with the resolution domain sides due to the particle propagation, but does not depend on the physical scale.

Our typical simulation scale is between 16 km^2 and 64 km^2 at resolutions between 512^2 and 4096^2 cells and sample counts as highlighted in Table 1. Our typical simulation time is between 10 and 1000 ky with time steps between 5 and 500 years.

The scenes we present in the following subsections require between 1000 and 4000 time steps to fully develop. With all additional overhead, the real runtime per iteration of the full erosion model

is 51 ms for a 1024^2 px terrain, resulting in overall simulation run times on the order of 1 to 10 minutes.

Table 1. Runtime performance of our algorithm, measured with NVIDIA Nsight Compute, taking the average of eight runs. We highlight the sample counts that we choose as a trade-off between performance and accuracy.

Samples N	512^2	1024^2	2024^2	4096^2
$8192 = 2^{14}$	1.1 ms	2.0 ms	3.9 ms	8.6 ms
2^{15}	1.2 ms	2.0 ms	3.9 ms	9.4 ms
2^{16}	1.1 ms	2.1 ms	4.2 ms	11.4 ms
2^{17}	1.2 ms	3.0 ms	6.2 ms	18.6 ms
2^{18}	3.0 ms	6.1 ms	12.4 ms	36.1 ms

Unless specified otherwise, we used parameters from Table 3 in Appendix C ($1024\,\text{px}^2$, 250 ky for 2000 iterations), and report the individual simulation times and runtime of each scene in Table 2.

Stability. The transport scheme is unconditionally stable. Local instabilities can occur in the erosion model, as we use explicit time-stepping for Eq. 1 and rely on solutions from previous iterations to express non-linear source and decay terms. The time step is thus limited numerically by instabilities in the erosion stepping, and phenomenologically by the quasi-static transport assumption, which does not hold under large variations, *e.g.* of the elevations.

Termination. Terrain erosion simulations are commonly terminated when the height-field reaches a steady-state permitted by the erosion law, *i.e.* when the uplift, erosion and deposition rates become balanced. In the morphological results, we choose to terminate the simulation early to showcase transient morphologies or interest, such as cliffs and shallow deposition fans.

Additionally, such a steady-state commonly exists in the absence of deposition instabilities. Our dynamic velocity field enable enhanced deposition patterns, but do not permit a clear steady-state in the sense of the SPL. Instead, we observe a *dynamic steady-state*, where the main slopes stabilize while flatter river trajectories oscillate. This can be observed in Fig. 9 and the companion video.

Table 2. Geological simulation time, timestep count and runtime for each reported scene.

Scene	Timesteps	Sim. Time	Runtime
Figure 3 (all)	2500	625 ky	128 s
Figure 4	3500	875 ky	178 s
Figure 5 (all)	2000	500 ky	100 s
Figure 6 (all)	1500	375 ky	76 s
Figure 7 (all)	800	200 ky	41 s
Figure 8	1000	250 ky	51 s
Figure 9 (all)	4000	1000 ky	204 s
Figure 10 (1024^2)	2500	500 ky	102 s

7.2 Eroded Landscapes and Morphological Results

Fig. 3 showcases varied results from our algorithm in three scenes, generated from a blank initial condition and various user-defined uplift, rainfall, and albedo maps as environmental boundary conditions, following the user controls from [Schott et al. 2023]. In particular, we design the scenes to show a large basin with converging streams (top), a rain shadow on a mountain range (middle), and a valley at a lower physical scale (bottom). Fig. 4 and the companion video show the evolution of a terrain over geological time scales.

We observe features characteristic of fluvial and debris flow erosion, with complex erosion and deposition patterns and stream morphologies. Areas of high uplift generate a large amount of material shedding, forming large and varied deposition patterns. High rainfall leads to dominant alluvial fans, and low rainfall leads to dominant debris fans. These deposits become layered and curved to conform to the uplift boundary condition, and are re-eroded towards the domain boundary, forming deep canyons, retreating cliffs, and stream banks. We observe streams merging into large rivers, covering entire basins. Momentum conservation influences river morphology everywhere, allowing for the emergence of braided patterns where high sediment loads meet shallow slopes, and meandering rivers that frequently switch path, leading to the emergence of fossilized riverbeds in the terrain.

Mountains exhibit multi-scale valley networks typical of fluvial erosion, as well as a multi-tiered slope distribution enhanced by erosion scars from debris-flow, as documented by Jain et al. [2024a].

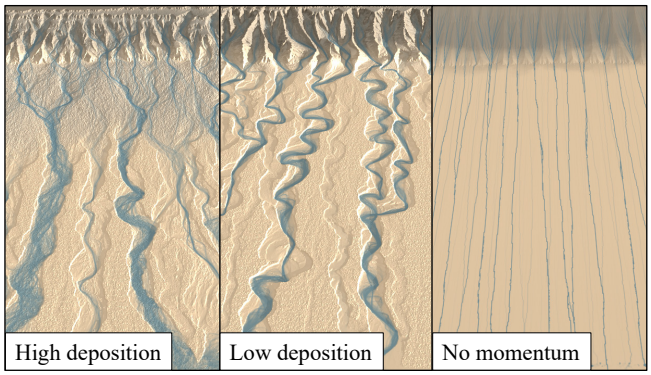

Fig. 5. Fluvial erosion momentum ablation. Our model produces braided rivers and meanders (left). Decreased deposition reduces momentum instabilities, eliminating braided patterns (middle). Without momentum conservation, meanders disappear and streams have no width (right).

7.3 Validation and ablation of the erosion model

We validate our erosion model through the observation of natural patterns emerging from our simulation. We conduct an ablation to highlight the parameters responsible for each of these patterns.

Meanders, braids and deltas. Under momentum conservation coupled with deposition dynamics, stream networks develop complex, multi-directional flow patterns such as braids, deltas, and meandering. Fig. 5 (left) shows these patterns in the deposit region at the foot of a mountain range, while the center and right images highlight the parameters responsible for this effect. Decreasing the deposition rate (center) reduces momentum instabilities and disables the formation of braids and deltas. Then, we remove the viscosity

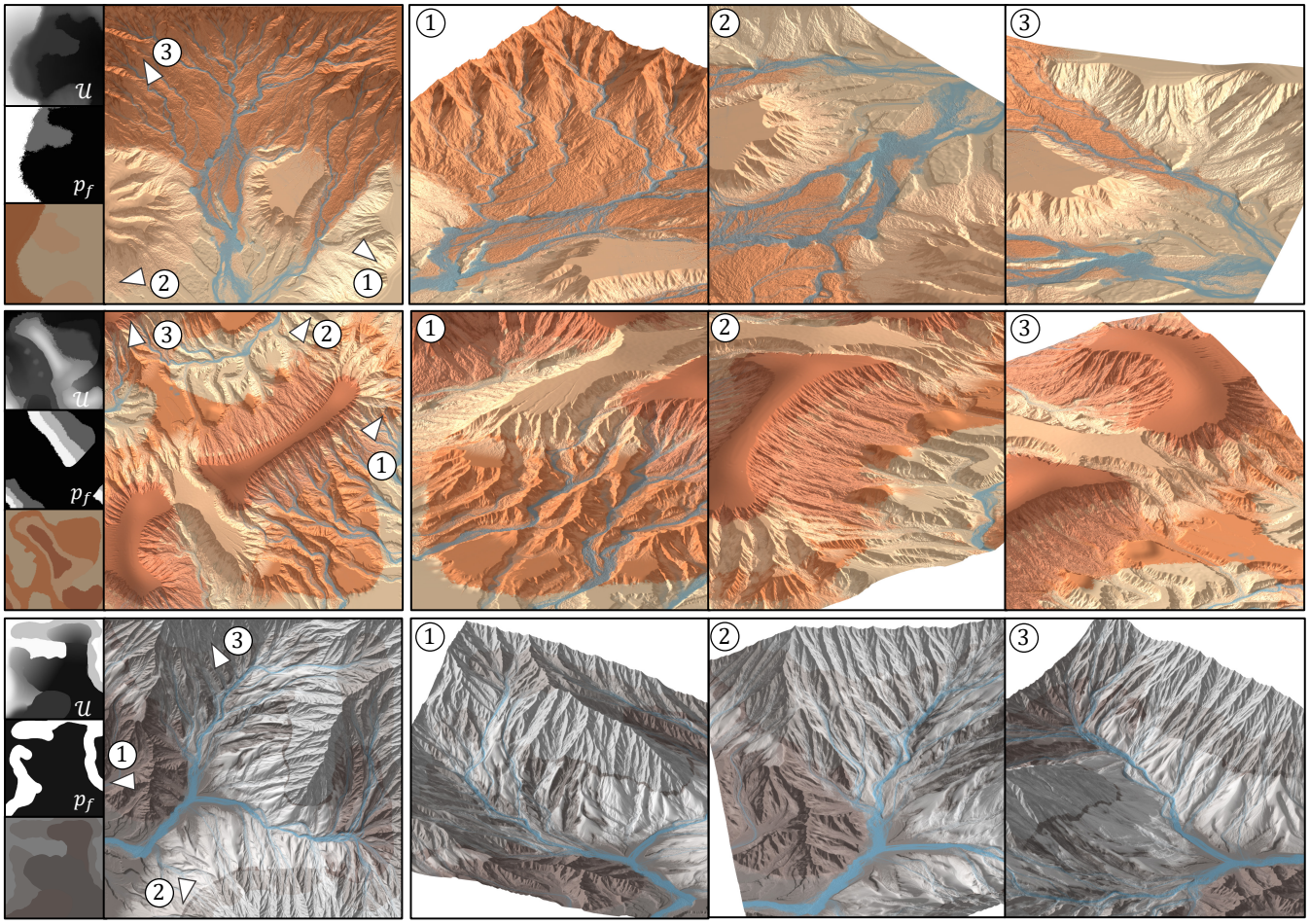

Fig. 3. Morphological outputs of our erosion model for various uplift, rainfall and albedo boundary conditions (far left, top to bottom) at different physical scales (top to bottom: 64 km^2, 64 km^2, 16 km^2). The close-up views showcase small- and large-scale river braiding, meandering streams, dry historical river paths, large re-eroded fluvial and debris deposition fans, plateaus with retreating escarpments and canyons. The deposition patterns exhibit complex curved shapes, conforming to the constraining uplift boundary condition, and can be observed layering on top of each other while also being eroded away.

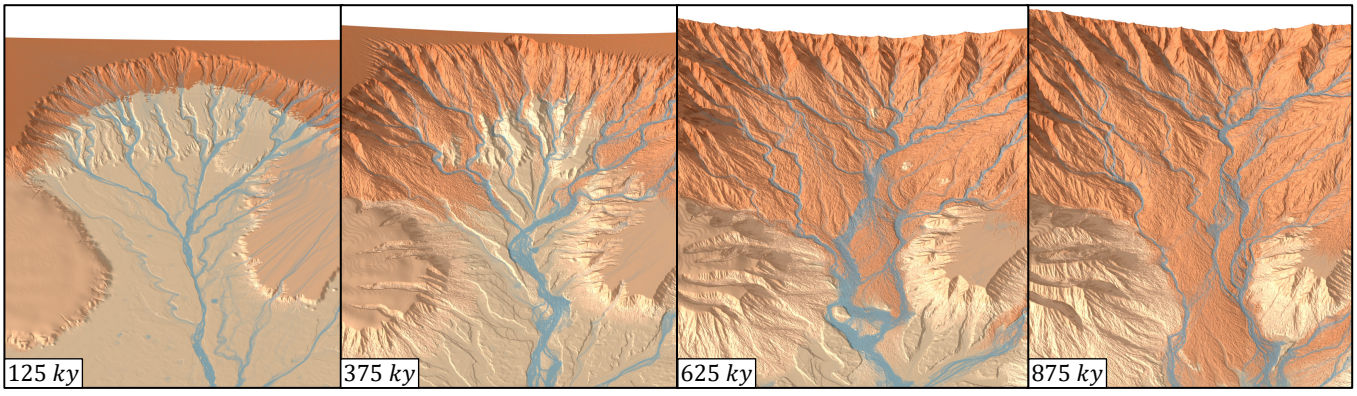

Fig. 4. Full erosion model time-lapse after 125, 375, 625 and 875 kyears, from user-provided uplift and rainfall boundary conditions. Streams initially converge narrowly in a central basin, then broaden as their sediment load increases and finally diverge as the deposition fans dominate the topography. Regions of high uplift and rainfall shed large amounts of mass, creating large, progressively growing deposits. Regions of lower rainfall form retreating cliffs and canyons.

term and raise the riverbed wall shear stress to cancel the effect of momentum conservation, which disables all meandering patterns (right).

We note that since we do not model the formation of pools or lakes, *deltas* only form in shallow regions of high sediment load where the streams lose their momentum through viscous and friction forces. We observe this ephemerally in foothill deposition regions.

Debris flow. Another change in our erosion model compared to the one proposed by Jain et al. [2024b] is the expression of debris-flow erosion with a rheology mixing dry granular material with viscous flows (Eq. 8). We apply our debris flow model on a retreating cliff generated by an uplift discontinuity with a gradient orthogonal to the cliff face, to show the effect of varying uplift rates.

Fig. 6 shows the effect of momentum conservation on the debris deposition patterns. With our model, debris fans can exhibit varying slopes and sizes based on the momentum of the incoming material, generated by the slope and total mass. Without momentum, the deposits stabilize under a constant slope close to the cliff.

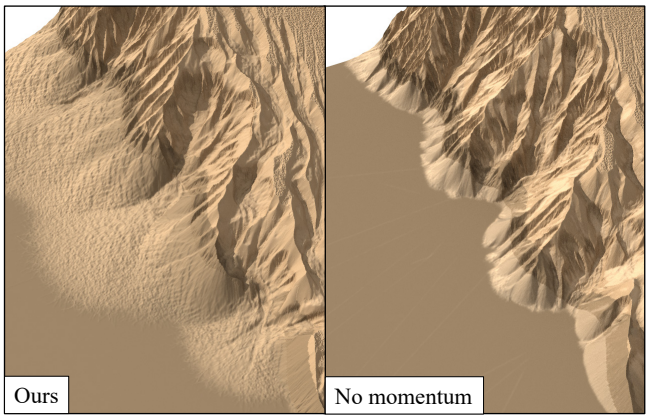

Fig. 6. Debris flow momentum ablation. The full model (left) exhibits debris fans of varying slope and extent. In the absence of momentum conservation, deposits only form at a single fixed slope (right).

Fig. 7 shows an ablation of the debris flow model to highlight the effect of each term in Eq. 8, in particular with increased landslide erosion rate k_l, debris erosion rate k_d, debris erosion rate $k_{d,d}$, and varying the debris erosion yield stress τ_y. Increasing the landslide erosion rate softens ridge-lines and decreases the equilibrium landslide slope, widening debris scars and shifting them towards higher uplift. A higher debris erosion rate decreases the scarring slope, broadening the erosion scars. A higher deposition rate increases deposit slope and decreases the deposit size. A higher yield stress increases the threshold for debris erosion, shifting the scars towards higher uplift, decreasing the slope and broadening the scars. A lower yield stress shifts the scars towards lower uplift while increasing the scarring slope, making them narrower.

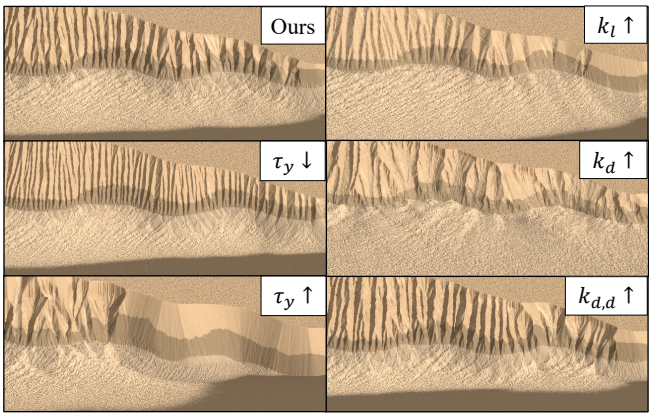

Fig. 7. Debris flow parameter ablation. Clockwise from top-left: Baseline model, higher landslide erosion rate, higher debris erosion rate, higher debris deposition rate, higher debris yield stress and lower debris yield stress.

Uniform Force. We show that momentum conservation enables additional user control through additional forces in Eq. 12. In Fig. 8, we add a uniform force field to the momentum conservation of the fluvial velocity $\mathbf{v}_f$, resulting in the formation of structures similar to *dune fields*. Indeed, the combination of a constant velocity with the topographic gradient in Eq. 12 mimics the wind-terrain interactions from previous wind erosion models [Paris et al. 2019]. While preliminary, this result gives a promising indication that our algorithm can efficiently incorporate wind- and ocean-related effects in a unified erosion model, for future work.

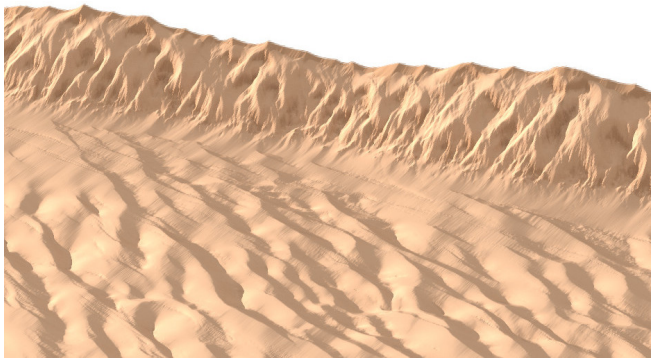

Fig. 8. Effect of an arbitrary lateral force-field applied to the fluvial transport model. Without modifying the erosion model, we observe patterns of wind erosion and the formation of structures similar to dune fields.

7.4 Comparisons

Models based on the Stream Power Law (SPL) on a regular grid [Jain et al. 2024a,b; Schott et al. 2023] tend to suffer from directional artifacts and strong self-similarities.

Fig. 9 compares close-up views of our results (left) and two variants using SPL: a version with momentum conservation on the velocity, but where the erosion itself follows the stream power law (middle), and a version where the velocity directly follows the topographic gradients (similar to [Jain et al. 2024b], right). We observe

that momentum conservation in the velocity solves the directional artifacts. Furthermore, our model which accounts for an explicit velocity model yields more diverse mountain distributions, compared to the regular slopes driven by the monotonicity of the stream power law. Finally, we notice that the model without momentum has narrower valley spacing, which indicates that valley spacing is controlled by momentum conservation in river trajectories.

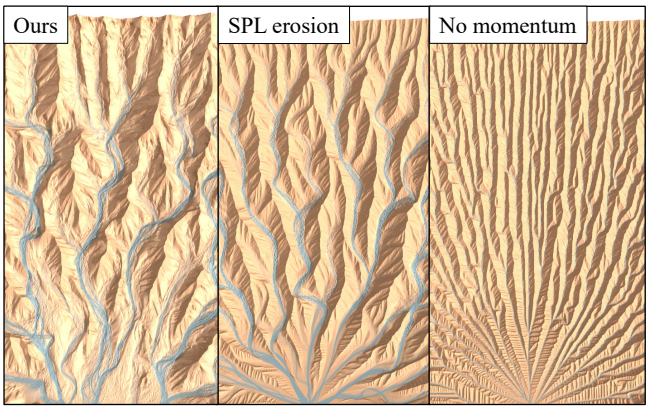

Fig. 9. A comparison of our velocity-based erosion model (left) with stream power law (SPL)-based erosion. The SPL exhibits monotone erosive power between valleys and ridges and excessive erosion in valleys, decreasing variability and lowering the amount and quality of deposits (middle). Without momentum, this leads to visible directional artifacting (right).

In Fig. 10, we compare our result across grids of different resolutions ($768\,\text{px}^2$, $1024\,\text{px}^2$, $1536\,\text{px}^2$) from the same blank initial condition, simulation time (500 ky) and sampling ratio (0.125), and show that our solution is more accurate and stable across scales – a property which is difficult to enforce with SPL-based approaches. Note that, while the deposition and stream patterns are highly similar across scales and long time scales, the solutions diverge slightly due to the absence of fine details and increased transport variance at lower resolutions. With a higher variance, the algorithm tends to overestimate transport, slightly increasing erosion rates.

Note that the improved patterns enabled by our method come at the cost of increased computational time. Compared to the most efficient GPU solver for the SPL, Fastflow [Jain et al. 2024b], which requires 2 ms for one iteration of flow routing (that models transport for the SPL) in a 1000×1000 terrain, our method requires in average 51 ms for solving both the fluvial and debris flow-transport on the same resolution at 2^{17} samples per iteration. Note that for a fair comparison, we did not count *depression routing* (15ms in Fastflow), although we observe that momentum conservation relaxes the strict need for depression management. The difference in performance is due to the graph reduction performed in $O(\log n)$ parallel iterations by Fastflow. In contrast, our method requires a number of iterations at worst proportional to the length of the longest path's resolution. In practice, this constraint is relaxed by terminating contributions which become attenuated below some threshold, i.e. the decay term R limits the maximum number of steps. Instead, our method is flexible in the number of samples chosen to compute the estimate for the transported quantities, offering a new avenue for control over the performance accuracy tradeoff.

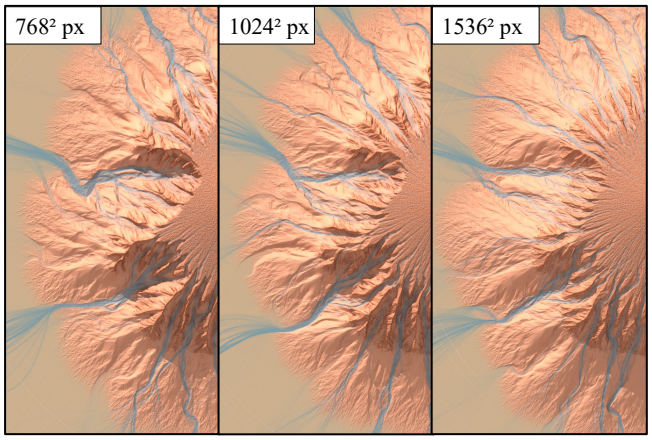

Fig. 10. Resolution invariance of the model for three resolutions (left to right: 768^2 px, 1024^2 px and 1536^2 px) at a constant sampling ratio of 0.125, simulated with the same initial and boundary conditions for 500 ky.

7.5 Applicability and limitations

Our primary assumption of geomorphological transport and the quasi-static approximation at the core of our model restrict it to phenomena that are instantaneous at the timescale of the erosion.

When this approximation is valid, the simplicity and flexibility of our model makes it easily applicable to a wide variety of phenomena, parameterizations and discretizations. Additional effects such as material mixture models or spatially varying erosion rates are easily achievable in our Lagrangian framework.

Conversely, our model is inaccurate for phenomena where this approximation is inacurate and the timescales match, for instance when erosion occurs rapidly at the scale of transport (*e.g.*, individual flooding or landslide events) or for transport which occurs slowly on the scale of erosion, (*e.g.*, glaciers).

8 CONCLUSION

We introduce a parallel, stochastic algorithm for *geomorphological transport* – the transport of erosional agents across a terrain over geological time scales. Our method enables the transport of velocity itself to enforce momentum conservation, enabling the formulation of a new erosion model based on flow velocities. Our results include highly detailed landscapes with patterns such as meanders or braided rivers and complex deposits, unattainable with previous methods for large-scale erosion. We show that the algorithm satisfies the underlying conservation equation, which ensures physical consistency and provides a basis for future extensions.

Our methodology opens new directions for the unified modeling a wide range of natural phenomena, such as dune and coastal erosion, rockfalls, floods, or underground water transfers. Future work includes improving sampling distributions, further GPU acceleration through graph reduction, or extensions to inverse models.

REFERENCES

Peter Ashmore. 1991. Channel morphology and bed load pulses in braided, gravel-bed streams. *Geografiska Annaler: Series A, Physical Geography* 73, 1 (1991), 37–52.

Bedrich Benes. 2007. Real-Time Erosion Using Shallow Water Simulation.. In *VRIPHYS*. 43–50.

Bedrich Benes and Rafael Forsbach. 2001. Layered Data Representation for Visual Simulation of Terrain Erosion. In *Proceedings of SCCG*, Vol. 25(4). IEEE Computer Society, 80–86.

Jean Braun and Sean D. Willett. 2013. A very efficient O(n), implicit and parallel method to solve the stream power equation governing fluvial incision and landscape evolution. *Geomorphology* 180-181 (2013), 170–179.

Clement G. Chase. 1992. Fluvial landsculpting and the fractal dimension of topography. *Geomorphology* 5, 1 (1992), 39–57. Fractals in Geomorphology.

M Hanif Chaudhry. 1979. *Applied hydraulic transients*. Springer.

Alex Chen, Jérôme Darbon, and Jean-Michel Morel. 2014. Landscape evolution models: A review of their fundamental equations. *Geomorphology* 219 (2014), 68–86.

Guillaume Cordonnier, Jean Braun, Marie-Paule Cani, Bedrich Benes, Eric Galin, Adrien Peytavie, and Eric Guérin. 2016. Large scale terrain generation from tectonic uplift and fluvial erosion. In *Computer Graphics Forum*, Vol. 35. Wiley Online Library, 165–175.

Guillaume Cordonnier, Marie-Paule Cani, Bedrich Benes, Jean Braun, and Eric Galin. 2017a. Sculpting mountains: Interactive terrain modeling based on subsurface geology. *IEEE transactions on visualization and computer graphics* 24, 5 (2017), 1756–1769.

Guillaume Cordonnier, Eric Galin, James Gain, Bedrich Benes, Eric Guérin, Adrien Peytavie, and Marie-Paule Cani. 2017b. Authoring landscapes by combining ecosystem and terrain erosion simulation. *ACM Transactions on Graphics (TOG)* 36, 4 (2017), 1–12.

Guillaume Cordonnier, Guillaume Jouvet, Adrien Peytavie, Jean Braun, Marie-Paule Cani, Bedrich Benes, Eric Galin, Eric Guérin, and James Gain. 2023. Forming Terrains by Glacial Erosion. *ACM Transactions on Graphics* 42, 4 (2023).

Philippe Davy, Thomas Croissant, and Dimitri Lague. 2017. A precipiton method to calculate river hydrodynamics, with applications to flood prediction, landscape evolution models, and braiding instabilities. *Journal of Geophysical Research: Earth Surface* 122, 8 (2017), 1491–1512.

David S. Ebert, Forest Kenton Musgrave, Darwyn Peachey, Ken Perlin, and Steven Worley. 2002. *Texturing and Modeling: A Procedural Approach*. Morgan Kaufmann Publishers Inc.

J. Gain, B. Merry, and P. Marais. 2015. Parallel, Realistic and Controllable Terrain Synthesis. *Computer Graphics Forum* 34, 2 (2015), 105–116.

Eric Galin, Eric Guérin, Adrien Peytavie, Guillaume Cordonnier, Marie-Paule Cani, Bedrich Benes, and James Gain. 2019. A review of digital terrain modeling. In *Computer Graphics Forum*, Vol. 38. Wiley Online Library, 553–577.

Éric Guérin, Julie Digne, Éric Galin, Adrien Peytavie, Christian Wolf, Bedrich Benes, and Benoît Martinez. 2017. Interactive Example-based Terrain Authoring with Conditional Generative Adversarial Networks. *ACM Transactions on Graphics* 36, 6, Article 228 (Nov. 2017), 13 pages. https://doi.org/10.1145/3130800.3130804

Andrew J. Guswa, M. A. Celia, and I. Rodriguez-Iturbe. 2002. Models of soil moisture dynamics in ecohydrology: A comparative study. *Water Resources Research* 38, 9 (2002), 5–1–5–15.

Eric Guérin, Adrien Peytavie, Simon Masnou, Julie Digne, Basile Sauvage, James Gain, and Eric Galin. 2022. Gradient Terrain Authoring. *Computer Graphics Forum* 41, 2 (2022), 85–95.

Marc Hartley, Nicolas Mellado, Christophe Fiorio, and Noura Faraj. 2024. Flexible terrain erosion. *The Visual Computer* 40, 7 (2024), 4593–4607.

Alan D. Howard and Gordon Kerby. 1983. Channel changes in badlands. *GSA Bulletin* 94, 6 (06 1983), 739–752.

Richard M Iverson. 1997. The physics of debris flows. *Reviews of geophysics* 35, 3 (1997), 245–296.

Richard M. Iverson and Chaojun Ouyang. 2015. Entrainment of bed material by Earth-surface mass flows: Review and reformulation of depth-integrated theory. *Reviews of Geophysics* 53, 1 (2015), 27–58.

Aryamaan Jain, Bedrich Benes, and Guillaume Cordonnier. 2024a. Efficient debris-flow simulation for steep terrain erosion. *ACM Transactions on Graphics (TOG)* 43, 4 (2024), 1–11.

Aryamaan Jain, Bernhard Kerbl, James Gain, Brandon Finley, and Guillaume Cordonnier. 2024b. FastFlow: GPU Acceleration of Flow and Depression Routing for Landscape Simulation. In *Computer Graphics Forum*, Vol. 43. Wiley Online Library, e15243.

Douglas J. Jerolmack and David Mohrig. 2007. Conditions for branching in depositional rivers. *Geology* 35, 5 (05 2007), 463–466.

Peter Krištof, Bedrich Benes, Jaroslav Křivánek, and Ondřej Šťava. 2009. Hydraulic Erosion Using Smoothed Particle Hydrodynamics. *Computer Graphics Forum (Proceedings of Eurographics 2009)* 28, 2 (mar 2009), 219–228.

Randall J LeVeque. 2002. *Finite volume methods for hyperbolic problems*. Vol. 31. Cambridge university press.

Joshua Lochner, James Gain, Simon Perche, Adrien Peytavie, Eric Galin, and Eric Guérin. 2023. Interactive authoring of terrain using diffusion models. In *Computer Graphics Forum*, Vol. 42. Wiley Online Library, e14941.

F Kenton Musgrave, Craig E Kolb, and Robert S Mace. 1989. The synthesis and rendering of eroded fractal terrains. *ACM Siggraph Computer Graphics* 23, 3 (1989), 41–50.

Axel Paris, Eric Guérin, Pauline Collon, and Eric Galin. 2023. Authoring and Simulating Meandering Rivers. *ACM Trans. Graph.* 42, 6, Article 239 (Dec. 2023), 14 pages.

Axel Paris, Adrien Peytavie, Eric Guérin, Oscar Argudo, and Eric Galin. 2019. Desertscape simulation. In *Computer Graphics Forum*, Vol. 38. Wiley Online Library, 47–55.

Simon Perche, Adrien Peytavie, Bedrich Benes, Eric Galin, and Eric Guérin. 2023. Authoring terrains with spatialised style. In *Computer Graphics Forum*, Vol. 42. Wiley Online Library, e14936.

QuadSpinner. 2025. Gaea. https://quadspinner.com/

Hugo Schott, Axel Paris, Lucie Fournier, Eric Guérin, and Eric Galin. 2023. Large-scale terrain authoring through interactive erosion simulation. *ACM Transactions on Graphics* 42, 5 (2023), 1–15.

World Machine Software. 2025. World Machine. www.world-machine.com

Philippe Steer. 2021. Short communication: Analytical models for 2D landscape evolution. *Earth Surface Dynamics* 9 (09 2021), 1239–1250. https://doi.org/10.5194/esurf-9-1239-2021

Petros Tzathas, Boris Gailleton, Philippe Steer, and Guillaume Cordonnier. 2024. Physically-based analytical erosion for fast terrain generation. In *Computer Graphics Forum*, Vol. 43. Wiley Online Library, e15033.

Juraj Vanek, Bedrich Benes, Adam Herout, and Ondrej Stava. 2011. Large-Scale Physics-Based Terrain Editing Using Adaptive Tiles on the GPU. *IEEE Computer Graphics and Applications* 31, 6 (2011), 35–44.

Kelin X. Whipple and Gregory E. Tucker. 1999. Dynamics of the stream-power river incision model: Implications for height limits of mountain ranges, landscape response timescales, and research needs. *Journal of Geophysical Research: Solid Earth* 104, B8 (1999), 17661–17674.

Chris Wojtan, Mark Carlson, Peter J. Mucha, and Greg Turk. 2007. Animating corrosion and erosion. In *Proceedings of the Third Eurographics Conference on Natural Phenomena* (Prague, Czech Republic) *(NPH'07)*. Eurographics Association, Goslar, DEU, 15–22.

Zhanyu Yang, Guillaume Cordonnier, Marie-Paule Cani, Christian Perrenoud, and Bedrich Benes. 2024. Unerosion: Simulating Terrain Evolution Back in Time. *Computer Graphics Forum* 43, 8 (2024), e15182. https://doi.org/10.1111/cgf.15182

Xiaoping P Yuan, Jean Braun, Laure Guerit, Delphine Rouby, and Guillaume Cordonnier. 2019. A new efficient method to solve the stream power law model taking into account sediment deposition. *Journal of Geophysical Research: Earth Surface* 124, 6 (2019), 1346–1365.

Howard Zhou, Jie Sun, Greg Turk, and James M. Rehg. 2007. Terrain Synthesis from Digital Elevation Models. *IEEE Transactions on Visualization and Computer Graphics* 13, 4 (2007), 834–848.

A DIVERGENCE OF ATTENUATED FLUX

Claim. We claim in Section 5 that $\hat{\phi}$ can alternatively be expressed as the divergence of the attenuated flux:

$$\nabla_{\mathbf{y}} \cdot (\alpha_C(\mathbf{y})\phi(\mathbf{y})\mathbf{v}(\mathbf{y})) = \hat{\phi}_C(\mathbf{y}), \tag{24}$$

where the divergence $\nabla_{\mathbf{y}}$ is taken with respect to the variable $\mathbf{y}$.

Proof. We apply the chain-rule to the divergence in Eq. 24:

$$\begin{aligned} &\nabla_{\mathbf{y}} \cdot (\alpha_C(\mathbf{y})\,\phi(\mathbf{y})\,\mathbf{v}(\mathbf{y})) \\ &\quad = \alpha_C(\mathbf{y})\nabla_{\mathbf{y}} \cdot (\phi(\mathbf{y})\mathbf{v}(\mathbf{y})) + (\phi(\mathbf{y})\mathbf{v}(\mathbf{y})) \cdot \nabla_{\mathbf{y}}\alpha_C(\mathbf{y}) \end{aligned} \tag{25}$$

We simplify the right-hand side of the sum in Eq. 25 with:

$$\alpha_C(\mathbf{y}) = \frac{M(\mathbf{x}_C)}{M(\mathbf{y})}, \tag{26}$$

and as $\mathbf{x}_C$ does not vary when $\mathbf{y}$ changes *over the streamline*,

$$\mathbf{v}(\mathbf{y}) \cdot \nabla_{\mathbf{y}} M(\mathbf{x}_C) = 0. \tag{27}$$

Then,

$$\begin{aligned} (\phi\mathbf{v})(\mathbf{y}) \cdot \nabla_{\mathbf{y}}\alpha_C(\mathbf{y}) &= M(\mathbf{x}_C)(\phi\mathbf{v})(\mathbf{y}) \cdot \nabla_{\mathbf{y}} \frac{1}{M(\mathbf{y})} \\ &= -\frac{M(\mathbf{x}_C)}{M(\mathbf{y})^2}(\phi\mathbf{v})(\mathbf{y}) \cdot \nabla_{\mathbf{y}} M(\mathbf{y}), \end{aligned} \tag{28}$$

and, using the definition of M (Eq. 14):

$$(\phi\mathbf{v})(\mathbf{y}) \cdot \nabla_{\mathbf{y}}\alpha_C(\mathbf{y}) = \alpha_C(\mathbf{y})R(\mathbf{y})\phi(\mathbf{y}) \tag{29}$$

We then substitute Eq. 13 in the left-hand side of the sum (we omit the variable $\mathbf{y}$ as there is no ambiguity remaining):

$$\nabla \cdot (\alpha_C\phi\mathbf{v}) = \alpha_C(S - R\phi) + \alpha_C R\phi - \alpha_C S = \hat{\phi}_C. \tag{30}$$

B INFLOW BOUNDARY CONDITION

In Section 4, we integrate Eq. 24 by applying Gauss' divergence theorem on a control volume Ω_C, defined as the union of the streamlines going through C. Assuming a smooth velocity field, the boundary of this domain is either C, or follows stream lines (connected to the extremities of C), or where $\mathbf{v} = 0$. One case remains, which is when the streamlines start from a boundary of the entire domain Ω, which then needs to be specified as an inflow boundary condition, located over $\mathcal{I}$:

$$\int_C \phi(\mathbf{y})\mathbf{v}(\mathbf{y}) \cdot \mathbf{dl}_{\mathbf{y}} = \int_{\Omega C} \hat{\phi}_C(\mathbf{y})\, dA_{\mathbf{y}} - \int_{\mathcal{I}} \alpha_C(\mathbf{y})\phi(\mathbf{y})\mathbf{v}(\mathbf{y}) \cdot \mathbf{dl}_{\mathbf{y}}. \tag{31}$$

In practice, we avoid an explicit treatment of the contributions from the inflow boundary. Instead, we treat them in the Monte-Carlo algorithm as another set of source terms, where $S = -\phi\mathbf{v} \cdot \mathbf{n}_{\mathbf{y}}$, where $\mathbf{n}_{\mathbf{y}}$ is the normal to $\mathcal{I}$ at $\mathbf{y}$. We use a specific probability $p_{\mathcal{I}}$ that particles start from points in the inflow boundary $\mathcal{I}$, and we weight the particles with $|\mathcal{I}|/p_{\mathcal{I}}$, where $|\mathcal{I}|$ is the length of $\mathcal{I}$. Finally, we set the initial velocity of these particles as specified in the boundary condition, instead of $\mathbf{v} = 0$ for the particles in the domain.

C SYMBOLS AND PARAMETERS

Table 3. Table of all symbols used in this work. Physical quantities are given with their units and parameters are provided with default values.

Symbol	Meaning	Value / Unit
Ω	Simulation Domain	
$\mathbf{x}$, $\mathbf{y}$	Horizontal Coordinates	
t	Simulation Time	
T	Simulation Duration	
z	Elevation	
$\mathcal{U}$	Tectonic Uplift Rate	$0.001\,\mathrm{m\,y^{-1}}$
$\mathcal{E}_f$, $\mathcal{E}_d$	Erosion Rate (Fluvial, Debris-Flow)	
$\mathcal{D}_f$, $\mathcal{D}_d$	Deposition Rate (Fluvial, Debris-Flow)	
$\mathcal{E}_l$	Erosion Rate (Landslide)	
$\mathbf{v}_f$, $\mathbf{v}_d$	Flow Velocity (Water, Debris)	$\mathrm{m\,s^{-1}}$
h_f, h_s, h_d	Flow Height (Water, Sediment, Debris)	m
τ_f, τ_d	Wall Shear Stress (Water, Debris)	Pa
ρ_f	Flow Density (Water)	$1000\,\mathrm{kg\,m^{-3}}$
ρ_d	Flow Density (Debris)	$2500\,\mathrm{kg\,m^{-3}}$
f_D	Darcy-Weisbach Friction Factor	0.06
a	Fluvial Erosion Exponent	2
k_f	Fluvial Suspension Coefficient	$4.5 \cdot 10^{-8}$
$k_{d,f}$	Fluvial Deposition Coefficient	0.05
k_l	Landslide Suspension Rate	0.0025
g	Specific Gravity	$9.81\,\mathrm{m\,s^{-2}}$
θ	Angle of Repose	37 Degrees
k_d	Debris Suspension Rate	0.01
$k_{d,d}$	Debris Deposition Rate	0.05
τ_y	Debris Surface Yield Stress	2 MPa
μ_f	Dynamic Viscosity (Fluvial)	0.001 Pa s
μ_d	Dynamic Viscosity (Debris)	0.004 Pa s
p_f	Precipitation Rate	$1\,\mathrm{m\,y^{-1}}$
k_e	Evapotranspiration Rate	$0.0005\,\mathrm{s^{-1}}$
$\nabla\cdot$	Divergence Operator	
Δ	Laplacian Operator	
ϕ	Transported Quantity / Material	
S	Material Source Term	
R	Material Decay Term	
M	Attenuation Function	
α	Attenuation Ratio	
$\hat{\phi}$	Attenuated Upstream Contribution	
C	Open Curve in Domain	
$\mathbf{dl}_{\mathbf{x}}$	Perpendicular Line Element	
A_y	Surface Element	
Ω_k	Discrete Cell in Domain	
ϕ_k	Transported Quantity in Cell	
O_k	Outflow Edge Set of Cell	
C_k	Outflow Open Curve of Cell	
Φ_k	Transport Integral Estimate	
$p(\mathbf{y})$	Joint Sampling Distribution	
ω_k	Upstream Indicator Function	
N	Total Sample Number	
Δt	Geological Timestep	250 y
β	Exponential Filter Rate	0.1